ARTICLE

Check for updates

Future changes in Antarctic coastal polynyas and bottom water formation simulated by a high-resolution coupled model

Hyein Jeong [1,2], Sun-Seon Lee [3,4], Hyo-Seok Park [1,2✉] & Andrew L. Stewart [5]

Antarctic coastal polynyas produce Dense Shelf Water, a precursor to Antarctic Bottom Waters that supply the global abyssal circulation. Future projections of Dense Shelf Water formation are hindered by unresolved small-scale atmosphere-sea ice-ocean interactions in polynyas. Here, we investigate the future evolution of Antarctic coastal polynyas using a high-resolution ocean-ice-atmosphere model. We find that wintertime sea ice production rates remain active even under elevated atmospheric CO_2 concentrations. Antarctic winter sea ice production rates are sensitive to atmospheric CO_2 concentrations: doubling CO_2 (734 ppm) decreases sea ice production by only 6–8%, versus 10–30% under CO_2 quadrupling (1468 ppm). While considerable uncertainty remains in future ice-shelf basal melting, which is not accounted for in this study, doubling or quadrupling CO_2 substantially freshens Dense Shelf Water due to increased precipitation. Consequently, doubling CO_2 weakens Dense Shelf Water formation by ~75%, while CO_2 quadrupling shuts down Dense Shelf Water formation.

[1] Institute of Ocean and Atmospheric Science (IOAS), Hanyang University, Ansan, South Korea. [2] Department of Marine Science and Convergence Engineering, Hanyang University, Ansan, South Korea. [3] Center for Climate Physics, Institute for Basic Science, Busan, South Korea. [4] Pusan National University, Busan, South Korea. [5] Department of Atmospheric and Oceanic Sciences, University of California, Los Angeles, CA, USA. ✉email: hspark1@gmail.com

A ntarctic coastal polynyas are areas of open water and thin, newly formed sea ice surrounded by coastline or ice shelves and consolidated thick sea ice[1]. They form where sea ice motion is divergent, typically as a consequence of strong offshore winds[2,3]. Although coastal polynyas occupy a relatively small proportion of the Antarctic sea ice area, they play an important role in regional climate by transporting heat from the ocean to the atmosphere, which affects mesoscale atmospheric motions[4,5]. More importantly, sea surface cooling and sea ice formation with brine rejection lead to Dense Shelf Water (DSW) formation[2,6–8]. DSW can lead to the formation of Antarctic Bottom Water (AABW) when it descends the continental slope and mixes with ambient water masses[7–10]. AABW production is a key element of the Earth's climate system on centennial to millennial timescales[9,11–13] and serves as an important sink for atmospheric CO_2 and heat[14–18]. Observational studies suggest that AABW volume may have been reduced over the recent decades because of Antarctic coastal freshening and warming[19–21].

Predicting the DSW and AABW responses to future climate change is a challenging task. A recent study suggests that retreating sea ice is likely to substantially weaken open-ocean convection in the Weddell Sea[22]. Predicting changes in Antarctic coastal convection is more challenging because coupled climate models with a relatively high grid resolution[23], ice-shelf basal melting[24], and landfast sea ice processes[25] are needed to resolve coastal polynyas and dense water overflows. Most current climate models participating in Coupled Model Intercomparison Project Phase 6 (CMIP6, ref. [26]) have difficulty in simulating Antarctic coastal polynyas due to their relatively coarse horizontal resolutions[27,28]. In these coarse-resolution models, AABW is usually formed in open-ocean polynyas, particularly in the Weddell Sea, which contrasts with the multi-decadal re-occurrence of such polynyas in nature[27,28]. Recent studies using high-resolution ocean models forced by atmospheric boundary conditions[29–31] found that the AABW formation declines by ~40% within 50 years in response to meltwater forcings in the highest-emission scenario (RCP8.5 or SSP5-8.5; ref. [32]).

In a high-resolution atmosphere-ocean coupled climate model, the zonal-mean meridional overturning circulation in the Southern Ocean is reduced by around 50% in response to atmospheric CO_2 doubling[23] (relative to the 1990s CO_2 mixing ratio). While the heat budget analysis over the entire Southern Ocean indicates that the circulation weakening is mainly driven by reduced heat loss to the atmosphere[23], regional-scale surface heat flux responses remain elusive. Because surface heat fluxes are strongly constrained by sea ice cover in polar oceans[33], reliable projections of Antarctic sea ice are needed to better predict the responses of DSW and AABW to future climate change. Using a fully coupled high-resolution climate model, this study shows that the wintertime Antarctic coastal sea ice production rates decrease by only 6–8% in doubling CO_2 conditions (corresponding to a 2.5 °C increase of the global average surface air temperature relative to 16 °C; ref. [34]), and by 10–30% in quadrupling CO_2 conditions (5.1 °C). Despite the continued sea ice production, the freshening of DSW in response to doubling weakens DSW formation by ~75%, whereas quadrupling CO_2 leads to a shutdown of DSW, and thus AABW formation.

Results

Antarctic sea ice production. In this section, we diagnose sea ice production in Antarctic coastal polynyas in the control simulation, which is forced with a CO_2 concentration level of 367 ppm (see Methods for details). Then, we examine how it changes with increasing CO_2 concentrations. The control experiment simulates

localized sea ice production, with rates of up to 10–15 m year^{-1} along the Antarctic coasts, particularly in the Ross, Weddell, Prydz and Adélie Seas (Fig. 1a). The relatively high sea ice production rates occurring in coastal polynyas leads to DSW formation, which can be quantified via the water-mass transformation (WMT; refs. [23,35–42], see Methods for details) rate. Figure 1b shows that our model-simulated WMT rates from May to October are mostly positive, implying that the surface water-mass loses buoyancy and becomes denser via diabatic processes. In the regions of relatively high sea ice production (see Fig. 1a), the WMT rate is also relatively high. Consistent with a previous study[35], the WMT rates due to sea ice production explain almost 80–90% of total WMT rates.

This study focuses on the four major coastal regions where the DSW forms: Prydz Bay (known as Cape Darnley in observations), the Adélie Coast, and the Ross and Weddell Seas[6,43,44]. The control simulation shows that the high annual sea ice production rates in these regions are concentrated within ~20 km of the Antarctic coasts (Fig. 1c–f). Our simulations do not include landfast sea ice, which can facilitate sea ice formation in the coastal polynyas[45–47]. It is important to note that the technical implementation of landfast sea ice is currently challenging due to the lack of observational data, and as of now, no CMIP6 model incorporates landfast sea ice.

In Prydz Bay, where Cape Darnley Bottom Water forms, the grounded iceberg tongue (icecape) is a key component of DSW formation[48,49], as it blocks the westward advection of sea ice[50] and thereby promotes sea ice formation. While the discrepancy between the observed and model-simulated sea ice production in Prydz Bay is not large (151 ± 17 km^3 in CESM1 vs. 194 ± 19 km^3 in observations[48]), the simulated DSW formation rate is smaller than observations (Table 1). Due to the uncertainty in observation-based DSW formation rates, a direct comparison between our model simulations and observations is imperfect. In the Adélie Sea, where the Adélie Land Bottom Water forms, the Mertz Glacier Tongue (MGT) plays a major role in coastal sea ice production[51] by blocking sea ice advection from the east. Simulated sea ice production in CESM1, in which the MGT is not implemented, is less than half of the observed value in the Adélie Sea, although the CESM1-simulated DSW formation rate (0.13 ± 0.08 Sv) overlaps the range of observational estimates (0.1 ~ 0.5 Sv, Table 1).

In the Weddell Sea polynya (Fig. 1f), simulated sea ice production is four times larger than observations (Table 1). Due to the challenges in estimating sea ice thickness, observed sea ice productions over the Weddell Sea polynya have large uncertainties, leading to discrepancies among several observations[48,52,53]. Although there are discrepancies in regional-scale sea ice productions between CESM1 and observations, the discrepancy reduces in the case when sea ice productions over the four major coastal polynyas are added together. The total sea ice volume productions of the model and observations are about ~580 ± 93 km^3 and ~664 ± 76 km^3, respectively (Table 1).

In response to CO_2 doubling and quadrupling, the seasonal sea ice areas of all four coastal polynyas show delayed freeze-up in austral autumn, with changes that are most pronounced between March and May (Fig. 2a–d). In March, sea ice area starts to increase in the control simulation (black line in Fig. 2a–d) but the coasts become almost ice-free under CO_2 quadrupling (red line in Fig. 2a–d). The delayed autumn freeze-up is associated with increased upper ocean heat content (~250 m) in summer and autumn (Supplementary Fig. 1), which is consistent with the mechanism underlying delayed freeze-up in the Arctic Ocean[54,55]. In all four polynyas, the upper ocean warming in response to CO_2 doubling and quadrupling maximizes in summer, up to ~3.0 °C relative to the last 30 years of the control
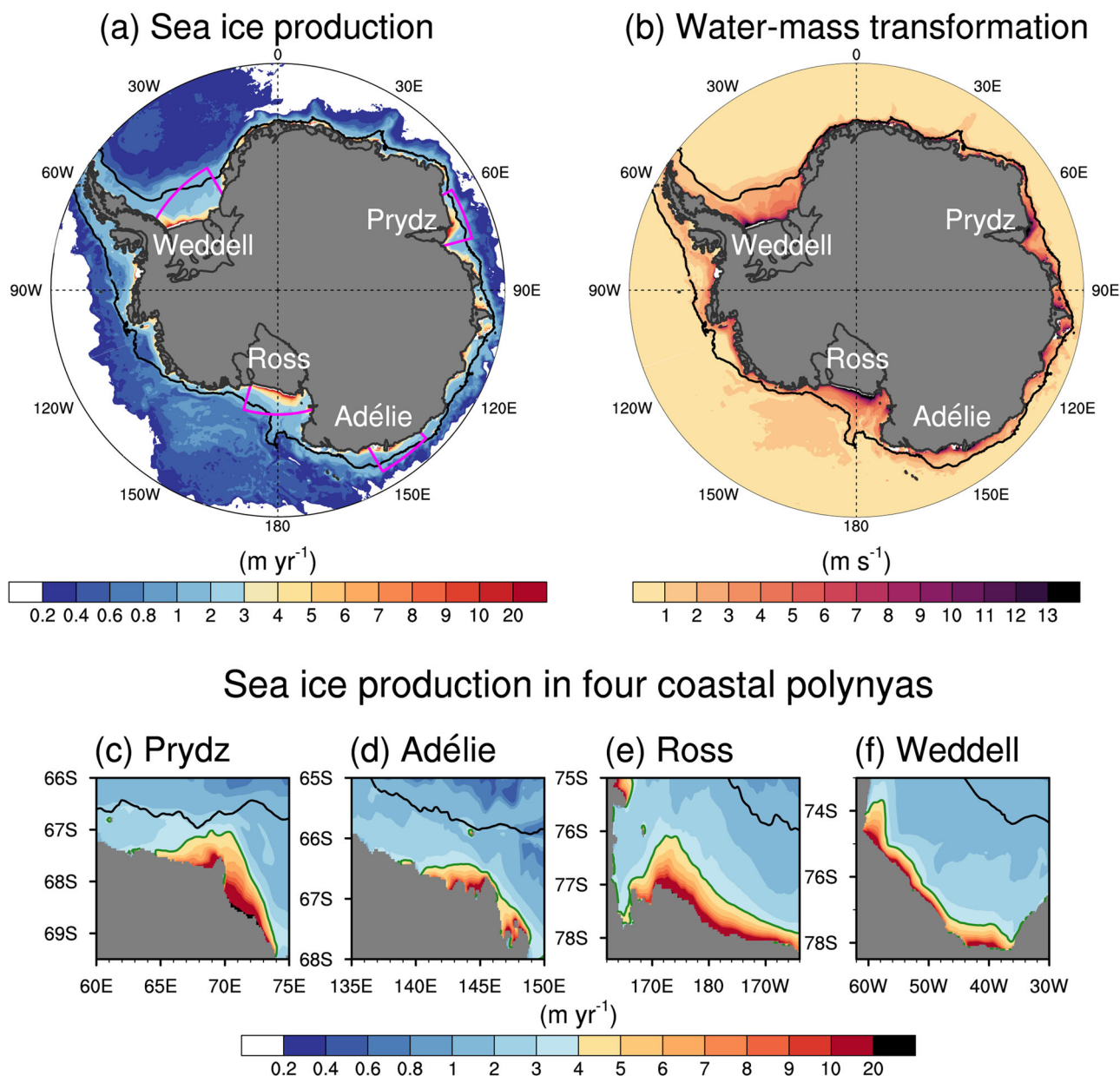
Fig. 1 Antarctic sea ice production and surface water-mass transformation. Climatological-mean winter (May–October) **a** sea ice production (m yr^{-1}) and **b** regional surface water-mass transformation rate (m s^{-1}) associated with sea ice formation, at potential density levels greater than 31.2 σ_1 (kg m^{-3}), simulated by the high-resolution coupled climate model with control simulation. Here, the regional surface water-mass transformation rate is divided by the area of each grid cell. (Bottom; **c**–**f**) Same as **a**, except for close-up views of **c** Prydz, **d** Adélie, **e** Ross, and **f** Weddell polynyas. Solid green lines bound the region in which sea ice production exceeds 4 m yr^{-1}. Black lines in each figure represent the 1000 m isobath. Pink outlines in **a** indicate four major coastal polynyas that this study focuses on.

simulation, indicative of increased absorption of shortwave radiation associated with decreased summer sea ice cover. In CO$_2$ quadrupling, 0.5–1.0 °C of positive upper ocean temperature anomalies persist into April and May.

Consistent with the upper ocean temperature anomalies (Supplementary Fig. 1), the freeze-up is delayed until around April in CO$_2$ doubling and until May in CO$_2$ quadrupling (Fig. 2a–d). However, sea ice area in both the CO$_2$ doubling and CO$_2$ quadrupling simulations almost reaches the level of the control simulation by mid-winter due to the seasonal northward growth of sea ice. In the Prydz Bay and Weddell Sea (Fig. 2a, d), the delayed autumn freeze-up is followed by a rapid increase in sea ice area, which recovers to match the sea ice area

of the control simulation in CO$_2$ doubling, but the level of recovery is limited to 85–90% of the control simulation in CO$_2$ quadrupling, primarily associated with sea surface warming along the northern margins of the Antarctic seas. Consistent with the sea ice area changes, the sea ice production starts about half a month delayed for the CO$_2$ doubling and a month delayed for the CO$_2$ quadrupling (Fig. 2e–h). In winter (June–September), during which sea ice production rates are highest, the CO$_2$ doubling leads to a moderate decline in sea ice production, by only ~6–8%. However, the CO$_2$ quadrupling leads to 10–30% decrease in sea ice production (Fig. 2i–l), highlighting the sensitivity of winter sea ice production to greenhouse gas emission scenarios.

Table 1 Climatological accumulated volume of sea ice production (km³) and DSW formation rate (Sv) during the winter season, along with annual standard deviations, in the Prydz, Adélie, Ross, and Weddell Sea polynyas from observed estimates and CESM1 control simulation.

		Observations	CESM1
Prydz	Sea ice production (km³)	194 ± 19	151 ± 17
	DSW formation (Sv)	0.3 ~ 0.7 (ref. [6])	0.05 ± 0.04
Adélie	Sea ice production (km³)	132 ± 19	51 ± 8
	DSW formation (Sv)	0.1 ~ 0.5 (ref. [44])	0.13 ± 0.08
Ross	Sea ice production (km³)	300 ± 22	218 ± 43
	DSW formation (Sv)	1.3 ~ 2.6 (ref. [43])	1.87 ± 0.30
Weddell	Sea ice production (km³)	38 ± 16	158 ± 24
	DSW formation (Sv)	4 ~ 5 (ref. [84])	2.50 ± 0.43

Surface heat fluxes. Changes in sea ice production rates are closely associated with changes in net surface heat flux. In response to CO_2 doubling, the wintertime surface air temperatures over the Prydz, Adélie, Ross, and Weddell Seas increase by 1.9 to 5.2 °C (Table 2), which can suppress surface heat loss to the atmosphere[23]. In response to increased surface air temperatures, wintertime (June–September) sea ice production rates in coastal polynyas are decreased in CO_2 doubling by 6–8% (Fig. 2i–l). Because the formation of coastal polynyas strongly depends on katabatic and synoptic winds[44], the strengthening of surface winds in response to global warming can enhance sea ice production. Although our model simulates a deepening of Antarctic low-pressure around the coasts in response to CO_2 doubling and quadrupling (Supplementary Fig. 2) (consistent with Southern Annular Mode strengthening under global warming[56–58]), we find that these pressure changes are not accompanied by
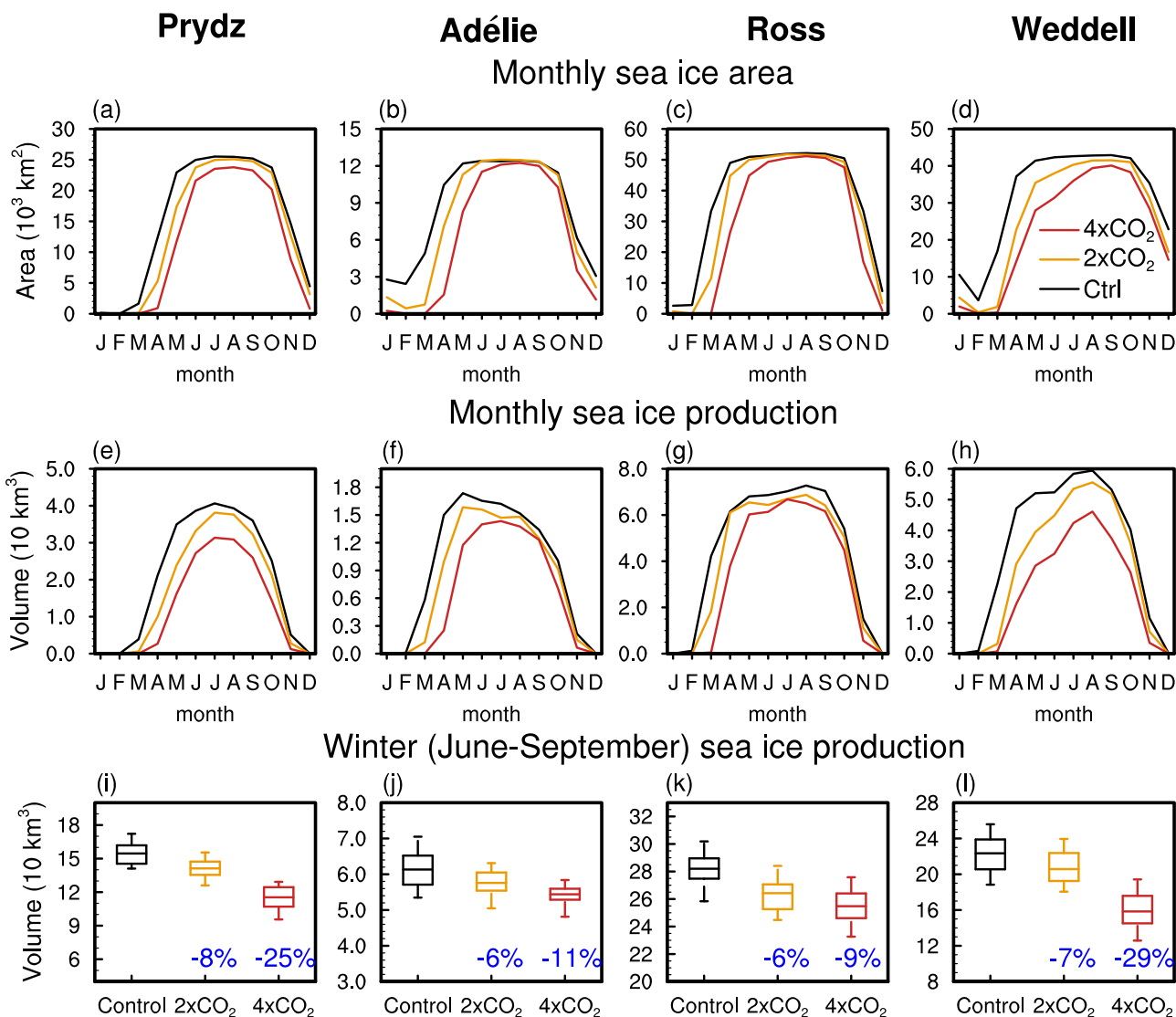

Fig. 2 Seasonal cycle of sea ice area and production in Control and increased CO₂ simulations. Climatological monthly-mean (top; **a–d**) sea ice area (10³ km²) and (middle; **e–h**) sea ice production (10 km³) over the Prydz, Adélie, Ross, and Weddell polynyas simulated by (black) Control, (orange) 2×CO₂, and (red) 4×CO₂ experiments. The abscissa is the time (month). Sea ice production rates are calculated within the coastal polynya boundaries from the Control simulation (solid green lines Fig. 1c–f). (bottom; **i–l**) The areally-averaged winter sea ice productions (accumulated from June to September) for the **i** Prydz, **j** Adélie, **k** Ross, and **l** Weddell polynyas, simulated by the (black) Control, (orange) 2×CO₂, and (red) 4×CO₂ experiments. Shown in each box plot are the median (middle solid line), the 25th and 75th percentile (lower and upper hinge), and the 5th and 95th percentiles (whiskers). Changes in median sea ice production rates relative to the Control simulation are given in blue text.

substantial changes in surface wind strength over the Antarctic coasts (Supplementary Fig. 2).

Another possible explanation for the modest reduction of sea ice formation under a CO_2 doubling is that reduced sea ice concentration (SIC) over the Antarctic coasts can increase heat loss to the atmosphere, partially offsetting the increase in surface air temperatures in warmer climates. Indeed, Fig. 3 shows that

Table 2 Climatological winter season (June–September) surface air temperatures (°C), averaged over the Prydz, Adélie, Ross, and Weddell polynyas (as indicated by the area shown in Fig. 1c–f) simulated by the Control, 2×CO_2, and 4×CO_2 experiments.

Coastal polynya	Control	2×CO_2	4×CO_2
Prydz	−19.9	−18.0 (1.9)	−13.9 (6.0)
Adélie	−22.7	−19.7 (3.0)	−16.7 (6.0)
Ross	−27.3	−23.9 (3.4)	−20.2 (7.1)
Weddell	−26.4	−21.2 (5.2)	−16.8 (9.6)

The values in parentheses in the 2×CO_2 and 4×CO_2 columns represent the surface temperature changes relative to the Control experiment.

daily net surface heat flux is negatively correlated with SIC over the four polynyas. Here, net surface heat flux ($NetFlux^\uparrow$) includes all the heat and radiative fluxes over both sea ice and open water:

$$NetFlux^\uparrow = SHF^\uparrow + LHF^\uparrow + LW^\uparrow - LW^\downarrow + SW^\uparrow - SW^\downarrow,$$
(1)

where, $SHF^\uparrow$ and $LHF^\uparrow$ denote upward sensible and latent heat fluxes, respectively, $LW^\uparrow$ and $LW^\downarrow$ represent upward and downward longwave radiative fluxes, respectively, and $SW^\uparrow$ and $SW^\downarrow$ represent upward and downward shortwave radiative fluxes, respectively. The wintertime average SIC is very high because open waters in coastal polynyas freeze-up rapidly[50]: a slight reduction of SIC, down to 80–90%, is followed by significant heat loss to the atmosphere in observations[59]. Consistent with observations, our model simulation shows that a decrease in SIC from 100% to 80% can effectively increase upward net surface heat flux to 40–90 W m^{-2} in all four polynya regions (Fig. 3a–d).

In warmer climates, grid cells with winter SIC lower than 60% occupy a larger proportion of the coastal areas (Fig. 3e–l), which may be expected to further increase the area-averaged surface temperatures. In response to CO_2 doubling, the sensitivity of the
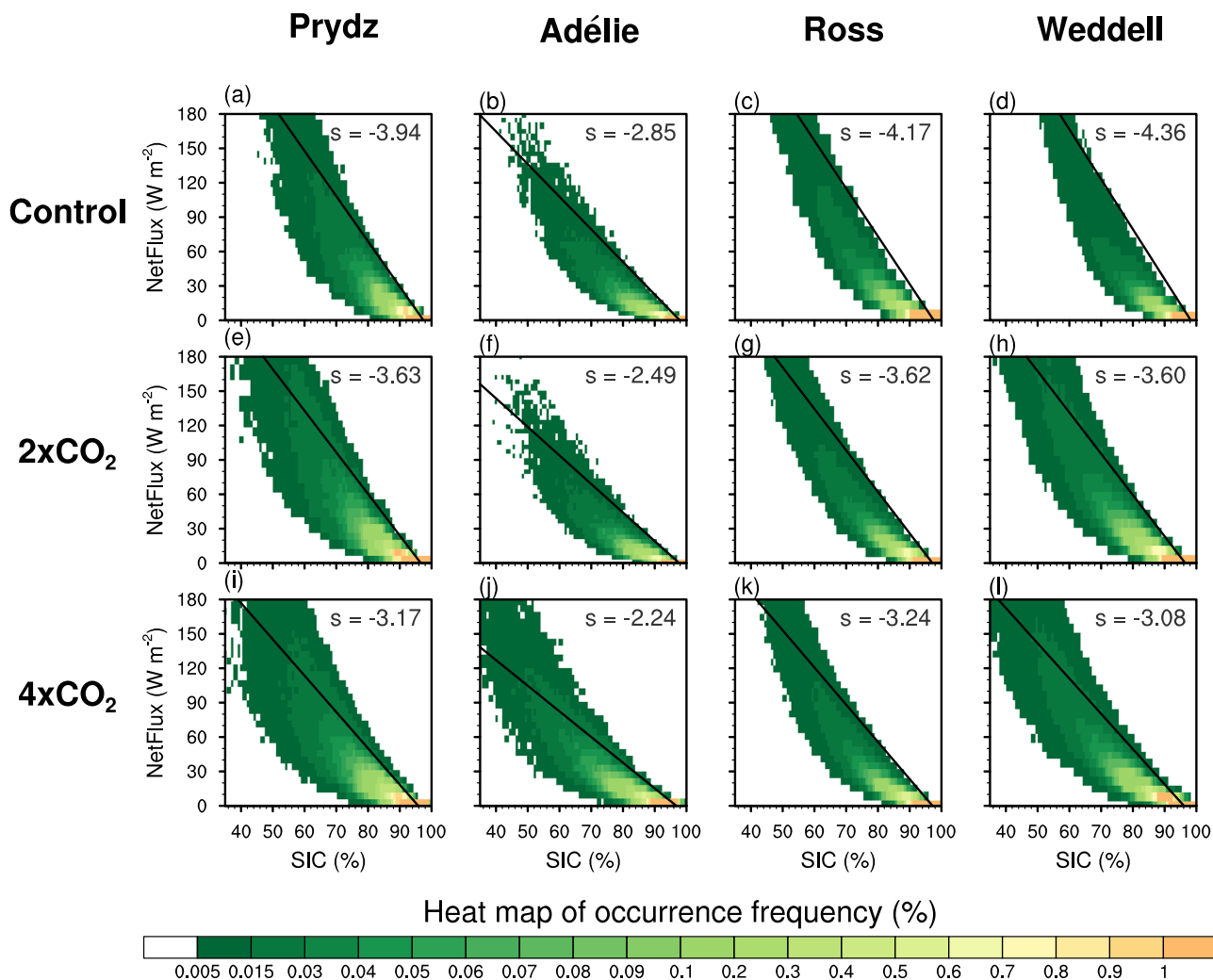

Fig. 3 Relationship between sea ice concentration and net surface heat flux. The probability distribution (frequency of occurrence) of the wintertime (June–September) daily net surface heat flux (NetFlux, W m^{-2}; ordinate) as a function of daily sea ice concentration (SIC,%; abscissa), calculated for each grid cell over the Prydz, Adélie, Ross, and Weddell Sea polynyas from the (top; **a–d**) Control, (middle; **e–h**) 2×CO_2, and (bottom; **i–l**) 4×CO_2 simulations. Solid black lines in each panel denote linear regression slopes from the Control, 2×CO_2, and 4×CO_2 simulations. The regression slopes (s; W m^{-2}%$^{-1}$) are calculated with grid cells of SIC larger than 15%. Positive heat flux implies heat flux from the ocean to the atmosphere.

ocean-to-atmosphere heat flux associated with decreasing SIC slightly weakens. In all four polynyas, the regression slopes in CO_2 doubling are about 8–16% smaller than the Control simulation (Fig. 3e–h). The sensitivity of the ocean-to-atmosphere heat flux to SIC further weakens in CO_2 quadrupling, being about 20–30% smaller than the Control simulation (Fig. 3i–l). These sensitivity changes might partly explain the differing responses of the wintertime sea ice production rates to different CO_2 increases, with little change for a medium-emission scenario and 10–30% reduction in a high-emission scenario (Fig. 2i–l).

Figure 4 indicates that the increased surface sensible heat flux ($SHF^\uparrow$) in response to decreasing SIC explains ~60–70% of the net surface heat flux sensitivity to SIC, i.e., the regression slopes in Fig. 4 are ~60–70% of those in Fig. 3. To aid conceptual understanding of the changing regression slopes in Fig. 4, we propose a simple 1D model for surface sensible heat flux over coastal polynyas. Assuming that sensible heat loss over the sea ice-covered fraction of the water is negligible (as the sea ice skin temperature is very close to the air temperature), the wintertime surface sensible heat flux can be re-written as a function of SIC

utilizing a bulk formula:

$$SHF^\uparrow = \rho_a c_p C_D U_{10} (T_s - T_a) \approx \rho_a c_p C_D U_{10} \left(1 - \frac{SIC}{100\%}\right)(T_f - T_a),$$

$$(2A)$$

where U_{10}, T_S, and T_a are wind speed at 10 m height, surface temperature, and surface air temperature, respectively. T_f is freezing temperature of seawater, which is set to $-1.8\,°C$. ρ_a is surface air density ($1.275\ kg\,m^{-3}$) and c_p is the specific heat capacity of air ($1005\ J\,kg^{-1}\,K^{-1}$). C_D is turbulent transfer coefficient over a partially sea ice-covered area, which is around 0.0015 (ref. [60]). Derivation of the above Eq. (2A) by SIC (%) leads to:

$$\frac{dSHF^\uparrow}{d\,SIC} \approx -\rho_a c_p C_D U_{10} \frac{(T_f - T_a)}{100\%} = \rho_a c_p C_D U_{10} \frac{(T_a - 1.8)}{100\%}$$
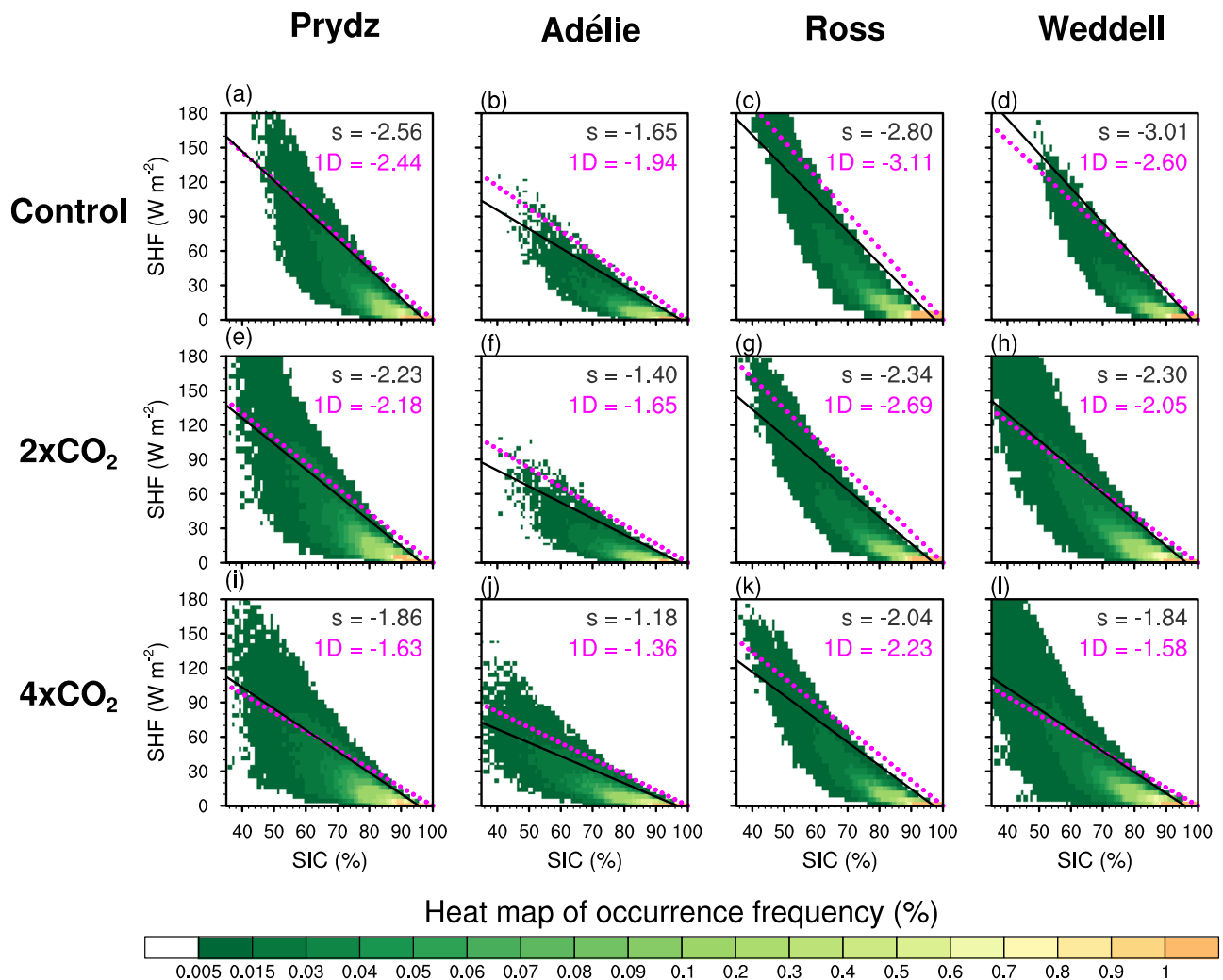
$$(2B)$$

Fig. 4 Relationship between sea ice concentration and surface sensible heat flux. The probability distribution (frequency of occurrence) of the wintertime (June–September) daily surface sensible heat flux (SHF, $W\,m^{-2}$; ordinate) as a function of daily sea ice concentration (SIC,%; abscissa), calculated for each grid cell over the Prydz, Adélie, Ross, and Weddell Sea polynyas from the (top; **a–d**) Control, (middle; **e–h**) 2×CO_2, and (bottom; **i–l**) 4×CO_2 simulations. Solid black lines in each panel denote linear regression slopes from the Control, 2×CO_2, and 4×CO_2 simulations. Dotted pink lines represent the sensitivity of surface sensible heat flux to sea ice concentration, estimated by Eq. (2B). The linear regression slopes (s; $W\,m^{-2}\%^{-1}$) between SIC and SHF are calculated with grid cells of SIC larger than 15%. Positive heat flux implies heat flux from the ocean to the atmosphere.

In the control simulation, for example, the wintertime T_a area-averaged over the Ross Sea is around $-27\ °C$ and T_a increases to around $-20\ °C$ in the CO_2 quadrupling. In terms of Eq. (2B), increasing T_a from $-27\ °C$ to $-20\ °C$ decreases the sensitivity of $SHF^{\uparrow}$ to SIC by ~28%, which is comparable to our model-simulated changes in the sensitivity (black line in Fig. 4k). In general, Eq. (2B) explains the sensitivity of net surface heat flux to SIC reasonably well: Similar to the black solid line (regression line) in Fig. 4, the slope of the pink dotted line also decreases with increased CO_2 simulation.

One of the limitations of this 1D linear model is that the sensitivities of net surface heat flux and SHF to SIC are not linear but slightly quadratic. Because the coastal polynyas are often driven by anomalously strong wind-driven ice flux divergence, there might be a correlation between U_{10} and SIC in Eq. (2A). While adding this negative correlation changes the linear relationship of Eq. (2A) into a quadratic relationship, the wind-driven formation of coastal polynyas occurs sporadically. At each grid cell, there is no statistically significant relationship between daily U_{10} and SIC in our model simulation, although the area-averaged U_{10} and SIC show a clear negative correlation (Supplementary Fig. 3). Another limitation of our 1D model is that sea ice thickness variation is not accounted for. While the formation of coastal polynyas is accompanied by ice thinning, net surface heat fluxes are far more sensitive to sea ice concentration than sea ice thickness (Supplementary Fig. 4). This is consistent with our conceptual 1D model that the majority of net surface heat flux can be estimated as a function of sea ice concentration.

Water-mass transformation and offshore transport. The active wintertime sea ice production in the coastal polynyas in warmer climates may be expected to provide favorable conditions for the maintenance of DSW production, despite the continuing sea surface freshening. The formation of dense water masses in coastal polynyas can be assessed by the WMT framework (see Methods for details), which relates surface density distributions and buoyancy fluxes to rates at which waters change their density at the interface between ocean and atmosphere, and between the ocean and sea ice.

Figure 5 shows the wintertime WMT rates as a function of potential density referenced to 1000 dB. In the control simulation, the formation of dense waters in Prydz Bay (consisting of Cape Darnley and Mackenzie Bay) amounts to 1.2 Sv (as indicated by the peak of the solid black line in Fig. 5a). In the Adélie Sea, the formation rate is ~0.5 Sv (Fig. 5b), somewhat smaller than those of other polynyas and but in agreement with an observation-
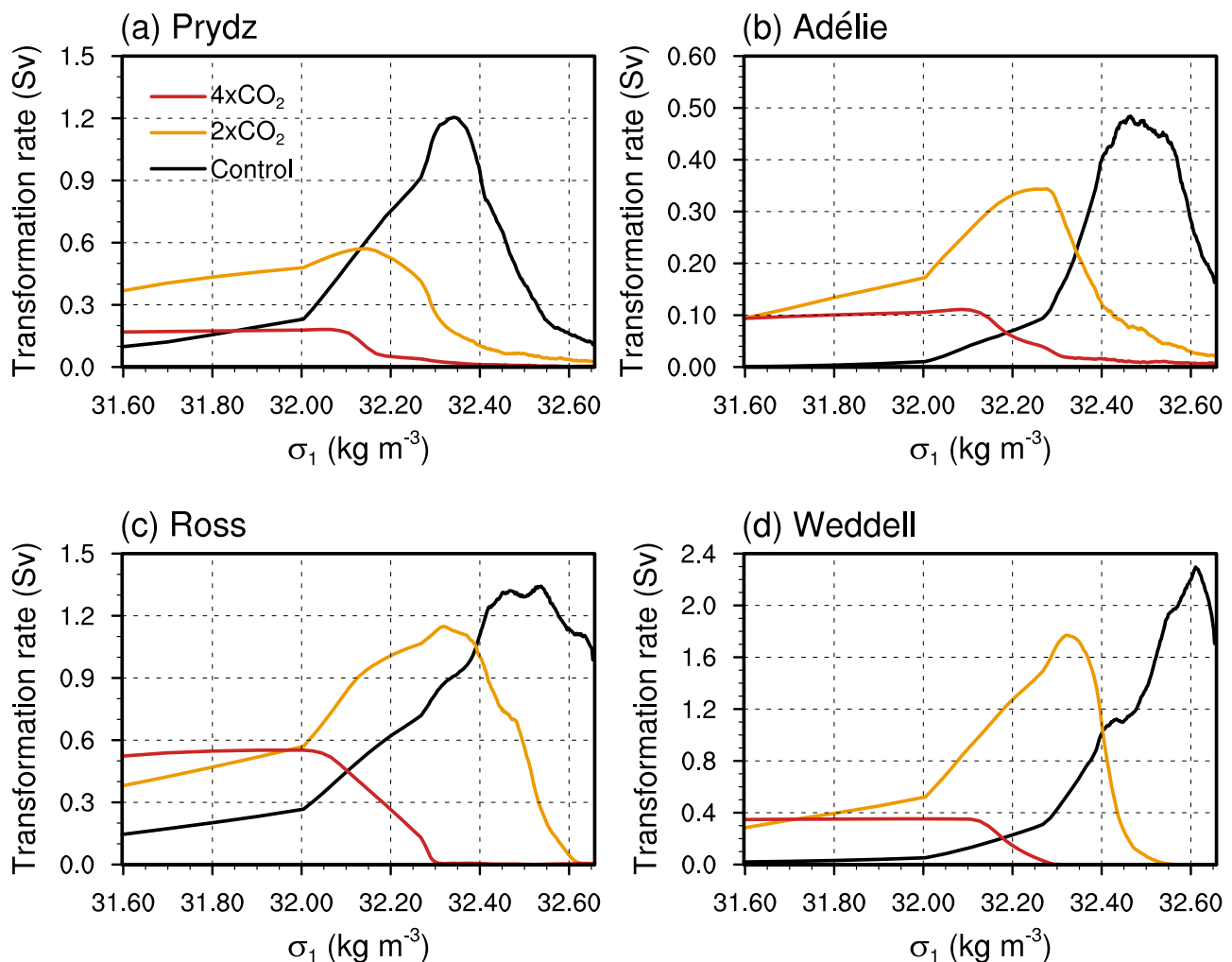

Fig. 5 Water-mass transformation rates in Control and warmer climate simulations. Thirty-year climatological winter season (June–September) water-mass transformation rates driven by total surface flux in the **a** Prydz, **b** Adélie, **c** Ross, and **d** Weddell polynyas in the (black) Control, (orange) 2×CO_2, and (red) 4×CO_2 simulations. The water-mass transformation rates are calculated over the polynya regions from the Control simulation (green lines in Fig. 1c–f).

based estimate[61]. Sea ice production is larger in the Ross Sea than in the Weddell Sea, which is generally consistent with observations[53]. However, the WMT rate associated with high surface density is higher in the Weddell Sea than in the Ross Sea (compare Fig. 5c, d). This implies that the WMT rate is not necessarily proportional to the sea ice production rate, but rather surface density distribution also plays a modulating role. Consistent with the shrinking areas of high sea ice production in warmer climates, the maximum WMT rates decrease by around 0.2–0.6 Sv under CO_2 doubling and by 0.4–2.0 Sv under CO_2 quadrupling in the four coastal polynyas.

The shift of dense water formation to lighter density classes as CO_2 increases implies that it becomes difficult for DSW to transform into AABW (ref. [31]). Figure 6 quantifies how much water-mass cascades down the continental slope and contributes to AABW in the control and increased CO_2 simulations. In the control simulation, shelf waters denser than $\sigma_1 = 32.38$ (the density at which the transport is maximum) flow offshore across

the 1000-m isobath in the amount of 6.7 ± 2.2 Sv (black line in Fig. 6b), which agrees well with observational estimates, 8.1 ± 2.6 Sv of AABW precursor waters[11,61]. Note that our simulated DSW outflow is somewhat smaller than that of other modeling studies using a high-resolution ocean-sea ice model[7,30], which simulates ~10.6 Sv of DSW outflow. However, ocean-sea ice models forced by atmospheric surface boundary conditions are known to overestimate coastal ice production and DSW outflows, because the lack of atmosphere-ocean coupling can overestimate sensible and latent heat fluxes from ocean to the atmosphere[4,38,62].

In the CO_2 doubling and quadrupling simulations, net offshore transports in higher density classes (denser than $\sigma_1 = 32.38$) rapidly decrease. They reduce to ~1.8 Sv under CO_2 doubling and ~0.03 Sv in CO_2 quadrupling (orange and red lines in Fig. 6b), suggesting CO_2 doubling decreases the export of newly formed DSW by around 75%, whereas CO_2 quadrupling leads to a shutdown of DSW export, and thus of AABW
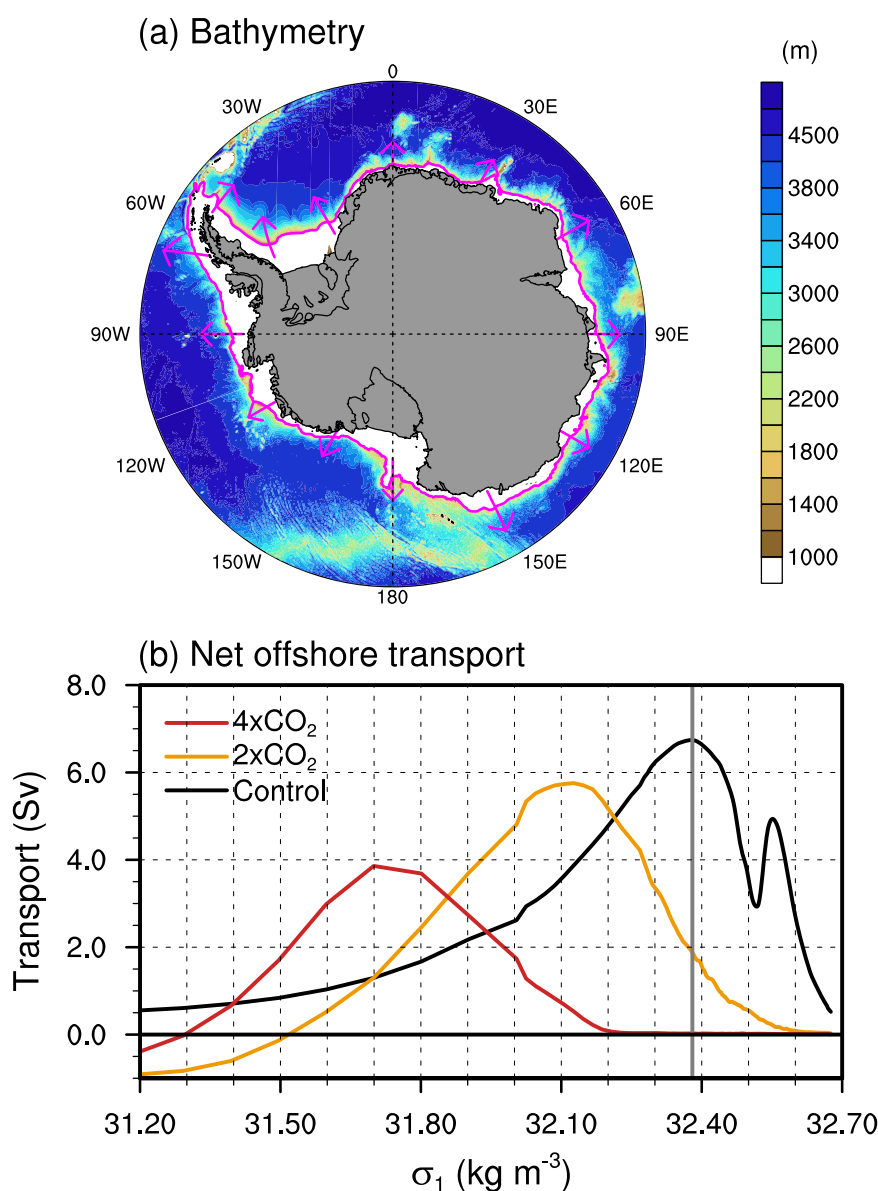

Fig. 6 Changes in net offshore transport. a Bathymetry in the abyss (m) from the Control simulation. Pink line in **a** represents the 1000 m isobath. Pink vectors denote offshore transport. **b** Net offshore transport across the 1000 m isobath, cumulatively summed in σ_1 space from high to low density from (black) Control, (orange) 2×CO_2, (red) 4×CO_2 simulations. The gray vertical line indicates the density threshold of DSW in the Control simulation. Positive and negative values mean offshore and onshore transport, respectively.

formation. These results are generally consistent with the changes in surface water-mass transformation rate in warmer climates (Fig. 5), showing that DSW denser than $\sigma_1 = 32.38$ does not form in the major coastal polynyas in the CO_2 quadrupling simulation.

Moreover, there is a clear shift of dense water formation and net offshore transport to lighter density classes as CO_2 increases, primarily because of decreasing sea surface salinity in coastal polynyas (Supplementary Fig. 5). Upper ocean freshening has multiple potential contributors, such as increased precipitation, increased freshwater discharge from the Antarctic continent, and melting ice shelves. In our CESM1 simulation, the freshwater discharge from Antarctica is calculated through "snow-capping" (see Method section), in which excess snow beyond 1.0 meter is discharged to the nearest ocean. In the CESM1 simulation, precipitation (mainly snowfall) increases by around 20–60% over the Antarctic continent and the Antarctic oceans in warmer climates (Fig. 7), which is consistent with previous modeling studies[63,64]. In the CMIP5 and CMIP6 ensembles, the highest-emission scenarios predict that Antarctic precipitation may increase approximately by 44-66% (ref. [64]), which is comparable to our high-resolution model response to CO_2 quadrupling. Consistent with our high-resolution model simulation (Fig. 7d, e), the increased precipitations in the CMIP5 and CMIP6 are found to be more prominent over the coastal margins than in the Antarctic continental interiors[64].

The increased snowfall is a key cause of sea surface freshening over the coastal polynyas, while meltwater from the adjacent Antarctic ice shelves is represented in an overly simplistic way via increased runoff from the Antarctic continent. The increased precipitation in the Weddell Sea coasts corresponds to 10 and 20 Gt year^{-1} of freshwater input in CO_2 doubling and quadrupling, respectively. These are far smaller than over 100 Gt year^{-1} of freshwater input over the southern Weddell Sea that has been estimated to result from increased ice-shelf melting in warmer climates[31]. Previous studies[31,37,39,65] have shown that future ice-shelf melting decreases sea surface salinity by around 0.1–0.3 PSU, although this estimate remains subject to significant uncertainties[31]. When considering the
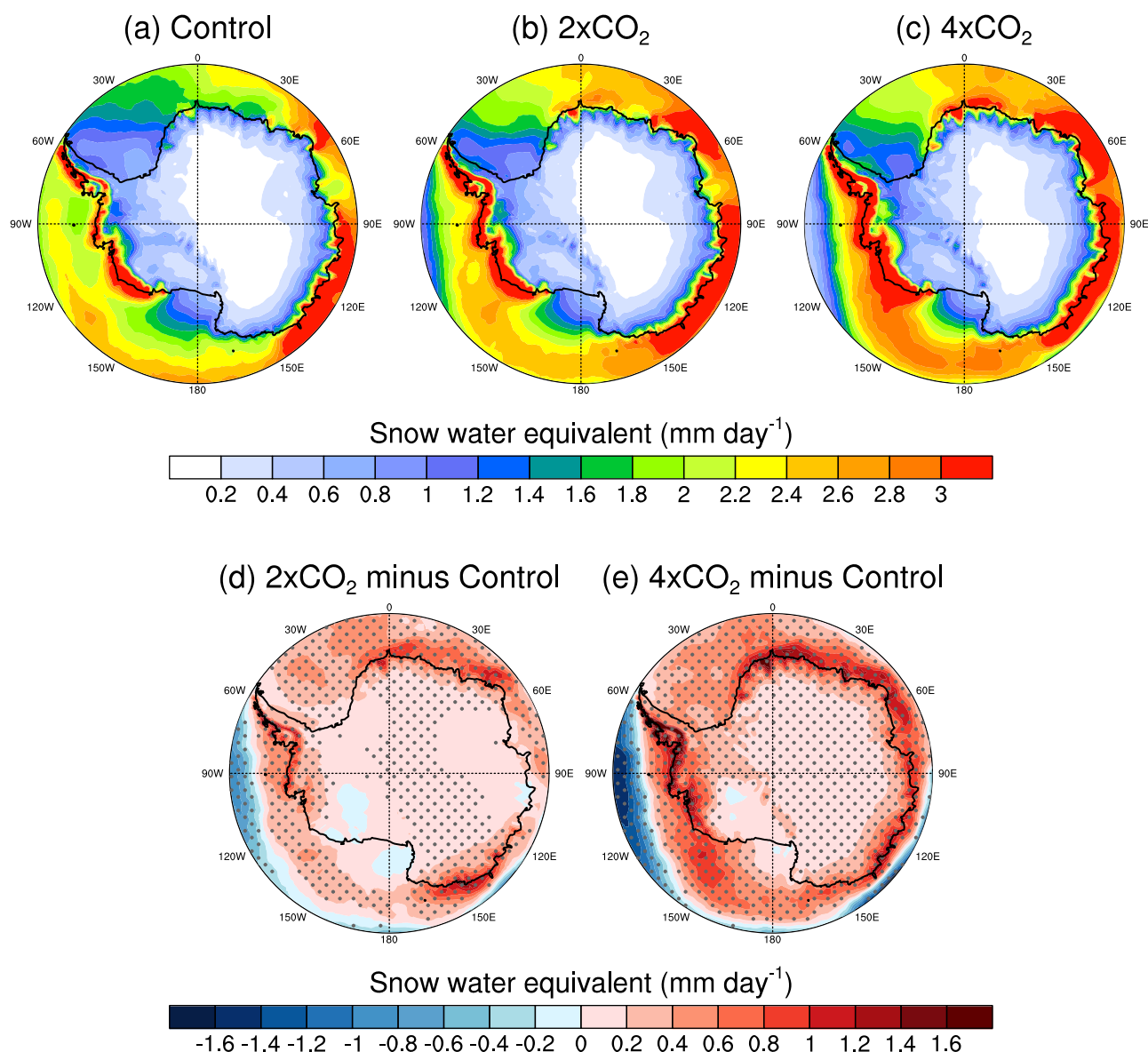

Fig. 7 Antarctic snowfall changes. (Upper; **a–c**) Climatological snow water equivalent (mm day^{-1}) in the winter (June–September) for **a** Control, **b** 2×CO_2, and **c** 4×CO_2 simulations. (Lower; **d**, **e**) Difference of climatological snow water equivalent **d** between 2×CO_2 and Control, and **e** between 4×CO_2 and Control simulations. **d**, **e** statistically significant values ($p < 0.05$) calculated from two-sample t test are stippled.

contribution of ice-shelf melting alongside precipitation changes, sea surface freshening is expected to intensify further.

Conclusions

Using a fully coupled high-resolution climate model that can resolve coastal polynyas, this study investigates how Antarctic coastal sea ice production and DSW formation respond to increasing greenhouse gas concentrations. Our model simulations suggest that delayed autumn freeze-up associated with increased upper ocean heat content substantially decrease the annual-mean sea ice area and sea ice production rates over Antarctic polynyas. However, the wintertime sea ice production rates decrease by only 6–8% in response to CO_2 doubling and 10–30% in response to CO_2 quadrupling. Modest sea ice reduction in warmer climates is mainly because the reduction in upward heat flux due to surface air warming is offset by decreasing sea ice cover, which effectively increases the mean surface temperature of the ocean/sea ice area. While the wintertime sea ice production in the coastal polynyas declines modestly in response to CO_2 doubling, the resulting density of newly formed DSW lightens due to surface freshening associated with increased precipitation rates. In response to CO_2 quadrupling, the wintertime sea ice production rates decrease further because surface air warming decreases the rate at which heat is lost to the atmosphere per unit of open-water area. Moreover, increased precipitation decreases surface salinity by ~0.7 PSU, further increasing the possibility of a shutdown of DSW formation.

While our model simulation reproduces the coastal sea ice production in the major polynyas well, the sensitivity of the sea ice production may depend on the sea ice model and parameter choices. Therefore, further studies with other high-resolution coupled models will be needed to establish a measure of uncertainty. We also acknowledge the limitations of our model configuration in this study, particularly the lack of ice-shelf melting that can cause further sea surface freshening around the Antarctic coasts. However, the impact of future ice-shelf melting has considerable uncertainty, not only in the amount of melting but also in the resulting sea surface freshening. Recent modeling studies[29,31,66] suggest that the accelerated ice-shelf melting can potentially lead to the shutdown of AABW when additional freshwater forcing is prescribed to the coastal sea surface or when ice-shelf melting is calculated dynamically. Although our CO_2 quadrupling simulation predicts substantial DSW freshening and a near-complete shutdown of AABW formation, we note that the low bias in AABW production in CESM1 (ref. [67]) may make the model artificially susceptible to a shutdown of AABW formation. Despite this limitation, our study provides a more realistic and comprehensive perspective on coastal sea ice production and DSW formation changes using a high-resolution coupled model, which simulates air-sea interactions in coastal polynyas.

Methods

High-resolution CESM coupled model simulations. The Community Earth System Model version 1.2.2 (CESM1.2.2) consists of coupled atmosphere (CAM5; Community Atmosphere Model version 5; ref. [68]), ocean (POP2; Parallel Ocean Program version 2; ref. [69]), land (CLM4; Community Land Model version 4; ref. [70]), and sea ice (CICE4; Community Ice CodE version 4; ref. [71]) components. We used the highest resolution "ne120_t12", in which CAM5 and CLM4 use a 0.25° (~25 km) and POP2 and CICE4 use a 0.1° (2.5 ~ 11 km) horizontal resolution. CAM5 has 30 vertical levels with model top at ~2 hPa and POP2 has 62 levels with a maximum depth of 6000 m. Our high-resolution model does not directly interact with Antarctic ice sheets/shelves, discharge from Antarctica is treated with snow-capping

parameterization. The snow-capping parametrization is activated whenever the snow depth in a grid cell exceeds a prescribed maximum value, set to 1 m in this study. Upon activation, the parameterization redistributes the excessive snow (ice flux) the ocean via a nearest-neighbor algorithm, spreading it using a Gaussian distribution over a radius of 300 km. If the ocean is warm enough, this ice flux is melted in the ocean immediately. These simplifications impose limitations on the potential evolution of excessive snowfall into glaciers. No overflow parameterization is employed in this study. We carried out three simulations with different CO_2 concentrations: (i) 367 ppm CO_2 concentration (Control simulation), (ii) CO_2 doubling ($2 \times CO_2$, 734 ppm), and (iii) CO_2 quadrupling ($4 \times CO_2$, 1468 ppm). All other greenhouse gas and aerosol concentrations were the same as in the control simulation. The Control simulation was initialized from a quasi-equilibrated climate state[72] and then integrated for another 140 years. The abrupt CO_2 doubling and quadrupling experiments were branched off from year 71 of the Control experiment and then integrated for 100 years each (see ref. [34] for details). Ref. [30] found a decline in AABW formation in response to meltwater forcings in RCP8.5 scenarios. Similarly, ref. [31] and ref. [29] obtained similar results to ref. [30] but used meltwater forcing with the SSP5-8.5 emission scenario. Both RCP8.5 and SSP5-8.5 scenarios project a CO_2 concentration increase up to 1100 ppm by 2100. The CO_2 quadrupling scenario, in this study, has a slightly higher CO_2 concentration than RCP8.5 or SSP5-8.5.

This study focuses on the Antarctic winter season, from May to October, during which the majority of sea ice production occurs. We examine the last 30 years of each simulation, discarding the first ~70 years of each simulation, to better focus on the equilibrium responses. Unless otherwise stated, all diagnostics used in the main text are drawn from the last 30 years of each simulation. Supplementary Fig. 6 illustrates how the seasonal Antarctic sea ice concentration is simulated in the high-resolution CESM1 with 367 ppm of CO_2 concentration. Our high-resolution CESM1-simulated Antarctic sea ice extent underestimates by ~40% compared to observed estimates; this underestimation appears in most climate models participated in CMIP5 (refs. [73,74]). Consistent with most models in CMIP5 and CMIP6 (refs. [75–79]), our high-resolution CESM1-simulated sea ice extent is sensitive to CO_2 increases, indicating annual-mean sea ice extent decreases by ~33% in CO_2 doubling and ~50% in CO_2 quadrupling. Our model simulation reproduces the seasonal variations in surface potential density referenced to 1000 dB, consistent with observations (Supplementary Fig. 7). As for seafloor temperature and salinity, our control simulation shows slightly warm and fresh bias near the key coastal polynyas. However, these biases are far smaller than CMIP6 multi-model averages (Supplementary Fig. 8). Simulated sea ice volume production integrated over the major four coastal polynyas in the control simulation is ~90% of the observed estimates (Table 1).

Surface flux-driven water-mass transformation. To better quantify the dense water formation in the Antarctic coastal polynyas, we apply a water-mass transformation framework (WMT; refs. [23,35–42]). WMT is defined as the volume flux of a water-mass consumed or produced by buoyancy forcing in each density class. Buoyancy forcing primarily occurs due to diapycnal mixing in the ocean interior and surface buoyancy fluxes, which is an exchange of buoyancy between the ocean and atmosphere or between the ocean and ice sheet/ice shelves. Our model configuration does not include the flux exchanging process between the ocean and ice sheet/ice shelves. This study

Table 3 Definition of parameters in Eq. (3).

Parameter	Description	Units
Ω	WMT rate	Sv ($10^6 \, \mathrm{m^3 \, s^{-1}}$)
σ_k	1000 dB-referenced potential density	$\mathrm{kg \, m^{-3}}$
t	Time	s
α	Thermal expansion	$\mathrm{kg \, m^{-3} \, K^{-1}}$
Q_{net}	Downward surface heat flux	$\mathrm{W \, m^{-2}}$
C_p	Specific heat of seawater (3994)	$\mathrm{J \, kg^{-1} \, K^{-1}}$
β	Haline coefficient of contraction	$\mathrm{kg \, m^{-3} \, psu^{-1}}$
F_{net}	Downward surface freshwater flux	$\mathrm{kg \, m^{-2} \, s^{-1}}$
S	Sea surface salinity	psu
ρ_0	Constant reference density of seawater (1035)	$\mathrm{kg \, m^{-3}}$
A	Horizonal ocean surface area of interest	$\mathrm{m^2}$

focuses on the transformation rate induced by surface heat and freshwater fluxes between the ocean and atmosphere/sea ice. The transformation across the density surface is diagnosed from surface heat and freshwater buoyancy fluxes:

$$\Omega(\sigma_k, t) = -\frac{1}{\sigma_{k+1} - \sigma_k} \iint_A \left(\frac{\alpha Q_{net}}{\rho_0 C_p} \right) dA$$
$$+ \frac{1}{\sigma_{k+1} - \sigma_k} \iint_A \left(\frac{\beta S F_{net}}{\rho_0} \right) dA, \quad (3)$$

where variables in Eq. (3) are defined in Table 3. The WMT is calculated numerically by discretizing potential density referenced to 1000 dB, σ_k, in 225 unevenly spaced bins from $1027.22 \, \mathrm{kg \, m^{-3}}$ to $1032.68 \, \mathrm{kg \, m^{-3}}$. The bin spacing, $\sigma_{k+1} - \sigma_k$, varies from $0.01 \, \mathrm{kg \, m^{-3}}$ at low densities to $0.002 \, \mathrm{kg \, m^{-3}}$ at high densities.

Offshore transport. To quantify how much water cascades down the continental slope, we calculate a net offshore transport across the 1000 m isobath around the Antarctic continental shelf. Following recent studies[7,30], the density characteristics of waters exchanged between the continental shelf and the open ocean are analyzed by binning daily averaged volume transports across the 1000 m isobath into potential density classes before taking an annual-mean and integrating time-averaged fluxes from high to low density.

$$T(\sigma_k, t) = \oint \vec{V} \cdot ds \quad (4)$$

where variables in Eq. (4) are defined in Supplementary Table 1. Similar to the WMT rate, the offshore transport is calculated in potential density space reference to 1000 dB, σ_k, in 225 unevenly spaced bins from $1027.22 \, \mathrm{kg \, m^{-3}}$ to $1032.68 \, \mathrm{kg \, m^{-3}}$. The bin spacing, $\sigma_{k+1} - \sigma_k$, varies from $0.01 \, \mathrm{kg \, m^{-3}}$ at low densities to $0.002 \, \mathrm{kg \, m^{-3}}$ at high densities.

Validation. Ocean temperature and salinity from the World Ocean Atlas 2018 (WOA18; refs. [80,81]) over the period 1995-2014 were utilized as a reference. To validate the CESM-simulated sea ice extent and concentration, we used the satellite-observed sea ice extent and concentration provided by the National Snow and Ice Data Center (NSIDC; refs. [82,83]).

Data availability

All data needed to evaluate the conclusions in the paper are present in the paper and/or the Supplementary Materials. The data from the high-resolution CESM simulations are available on the IBS Center for Climate Physics climate data server (https://climatedata.ibs.re.kr/). The ocean temperature and salinity from WOA18 can be accessed through https://www.ncei.noaa.gov/access/world-ocean-atlas-2018/. Sea ice concentration from NSIDC can be obtained from https://nsidc.org/data/G02202/versions/4.

Code availability

The CESM source code and the standard setup files for the high-resolution model simulation can be obtained from http://www.cesm.ucar.edu/models/cesm1.2/. The data analysis was conducted using the software CDO (https://code.mpimet.mpg.de/projects/cdo/embedded/cdo.pdf) and NCL (https://www.ncl.ucar.edu/). The source code for calculating the surface water-mass transformation rate can be found at https://github.com/hijeong820310/WaterMassTransformation.

References

1. Kusahara K., Hasumi H., Tamura T. Modeling sea ice production and dense shelf water formation in coastal polynyas around East Antarctica. *J. Geophys. Res.: Oceans* **115**, C10006 (2010).
2. Williams, W., Carmack, E. & Ingram, R. Physical oceanography of polynyas. *Elsevier Oceanogr. Ser.* **74**, 55–85 (2007).
3. Tamura, T., Ohshima, K. I., Fraser, A. D. & Williams, G. D. Sea ice production variability in Antarctic coastal polynyas. *J. Geophys. Res.: Oceans* **121**, 2967–2979 (2016).
4. Morales Maqueda M. A., Willmott A. J., Biggs N. Polynya dynamics: a review of observations and modeling. *Rev. Geophys.* **42**, RG1004 (2004).
5. Minnett, P. & Key, E. Meteorology and atmosphere–surface coupling in and around polynyas. *Elsevier Oceanogr. Ser.* **74**, 127–161 (2007).
6. Ohshima, K. I. et al. Antarctic bottom water production by intense sea-ice formation in the Cape Darnley polynya. *Nat. Geosci.* **6**, 235–240 (2013).
7. Morrison, A., Hogg, A. M., England, M. H. & Spence, P. Warm circumpolar deep water transport toward Antarctica driven by local dense water export in canyons. *Sci. Adv.* **6**, eaav2516 (2020).
8. Aoki, S. et al. Warm surface waters increase Antarctic ice shelf melt and delay dense water formation. *Commun. Earth Environ.* **3**, 142 (2022).
9. Williams, G. et al. The suppression of Antarctic bottom water formation by melting ice shelves in Prydz Bay. *Nat. Commun.* **7**, 12577 (2016).
10. Mensah, V., Nakayama, Y., Fujii, M., Nogi, Y. & Ohshima, K. I. Dense water downslope flow and AABW production in a numerical model: Sensitivity to horizontal and vertical resolution in the region off Cape Darnley polynya. *Ocean Modell.* **165**, 101843 (2021).
11. Orsi, A. H., Johnson, G. C. & Bullister, J. L. Circulation, mixing, and production of Antarctic Bottom Water. *Prog. Oceanogr.* **43**, 55–109 (1999).
12. Johnson G. C. Quantifying Antarctic bottom water and North Atlantic deep water volumes. *J. Geophys. Res.: Oceans* **113**, C05027 (2008).
13. Marshall, J. & Speer, K. Closure of the meridional overturning circulation through Southern Ocean upwelling. *Nat. Geosci.* **5**, 171–180 (2012).
14. Sigman, D. M. & Boyle, E. A. Glacial/interglacial variations in atmospheric carbon dioxide. *Nature* **407**, 859–869 (2000).
15. Mahieu, L., Lo Monaco, C., Metzl, N., Fin, J. & Mignon, C. Variability and stability of anthropogenic CO2 in Antarctic Bottom Water observed in the Indian sector of the Southern Ocean, 1978–2018. *Ocean Sci.* **16**, 1559–1576 (2020).
16. Sandrini, S. et al. Anthropogenic carbon distribution in the Ross Sea, Antarctica. *Antarct. Sci.* **19**, 395–407 (2007).
17. Shadwick, E., Tilbrook, B. & Williams, G. Carbonate chemistry in the Mertz Polynya (East Antarctica): biological and physical modification of dense water outflows and the export of anthropogenic CO2. *J. Geophys. Res.: Oceans* **119**, 1–14 (2014).
18. van Heuven, S. M., Hoppema, M., Jones, E. M. & de Baar, H. J. Rapid invasion of anthropogenic CO2 into the deep circulation of the Weddell Gyre. *Philos. Transact. A Math. Phys. Eng. Sci.* **372**, 20130056 (2014).
19. Rintoul S. R. Rapid freshening of Antarctic Bottom Water formed in the Indian and Pacific oceans. *Geophys. Res. Lett.* **34**, L06606 (2007).
20. Menezes, V. V., Macdonald, A. M. & Schatzman, C. Accelerated freshening of Antarctic Bottom Water over the last decade in the Southern Indian Ocean. *Sci. Adv.* **3**, e1601426 (2017).
21. Silvano, A. et al. Freshening by glacial meltwater enhances melting of ice shelves and reduces formation of Antarctic Bottom Water. *Sci. Adv.* **4**, eaap9467 (2018).
22. De Lavergne, C., Palter, J. B., Galbraith, E. D., Bernardello, R. & Marinov, I. Cessation of deep convection in the open Southern Ocean under anthropogenic climate change. *Nat. Clim. Change* **4**, 278–282 (2014).
23. Newsom, E. R., Bitz, C. M., Bryan, F. O., Abernathey, R. & Gent, P. R. Southern Ocean deep circulation and heat uptake in a high-resolution climate model. *J. Clim.* **29**, 2597–2619 (2016).
24. Nicholls K. W., Østerhus S., Makinson K., Gammelsrød T., Fahrbach E. Ice-ocean processes over the continental shelf of the southern Weddell Sea, Antarctica: a review. *Rev. Geophys.* **47**, RG3003 (2009).

25. Fraser, A. et al. Antarctic landfast sea ice: a review of its physics, biogeochemistry and ecology. *Rev. Geophys.* **61**, e2022RG000770 (2023).

26. Eyring, V. et al. Overview of the Coupled Model Intercomparison Project Phase 6 (CMIP6) experimental design and organization. *Geosci. Model Dev.* **9**, 1937–1958 (2016).

27. Heuzé, C. Antarctic bottom water and North Atlantic deep water in CMIP6 models. *Ocean Sci.* **17**, 59–90 (2021).

28. Mohrmann, M., Heuzé, C. & Swart, S. Southern Ocean polynyas in CMIP6 models. *Cryosphere* **15**, 4281–4313 (2021).

29. Li, Q., England, M. H., Hogg, A. M., Rintoul, S. R. & Morrison, A. K. Abyssal ocean overturning slowdown and warming driven by Antarctic meltwater. *Nature* **615**, 841–847 (2023).

30. Moorman, R., Morrison, A. K., McC & Hogg, A. Thermal responses to Antarctic ice shelf melt in an eddy-rich global ocean–sea ice model. *J. Clim.* **33**, 6599–6620 (2020).

31. Nissen, C., Timmermann, R., Hoppema, M., Gürses, Ö. & Hauck, J. Abruptly attenuated carbon sequestration with Weddell Sea dense waters by 2100. *Nat. Commun.* **13**, 3402 (2022).

32. O'Neill, B. C. et al. The scenario model intercomparison project (ScenarioMIP) for CMIP6. *Geosci. Model Dev.* **9**, 3461–3482 (2016).

33. Goosse, H. et al. Quantifying climate feedbacks in polar regions. *Nat. Commun.* **9**, 1919 (2018).

34. Chu, J.-E. et al. Reduced tropical cyclone densities and ocean effects due to anthropogenic greenhouse warming. *Sci. Adv.* **6**, eabd5109 (2020).

35. Abernathey, R. P. et al. Water-mass transformation by sea ice in the upper branch of the Southern Ocean overturning. *Nat. Geosci.* **9**, 596–601 (2016).

36. Pellichero, V., Sallée, J.-B., Chapman, C. C. & Downes, S. M. The southern ocean meridional overturning in the sea-ice sector is driven by freshwater fluxes. *Nat. Commun.* **9**, 1789 (2018).

37. Jeong, H. et al. Impacts of ice-shelf melting on water-mass transformation in the Southern Ocean from E3SM simulations. *J. Clim.* **33**, 5787–5807 (2020).

38. Jeong, H. et al. Southern Ocean polynyas and dense water formation in a high-resolution, coupled Earth system model. *Cryosphere* **17**, 2681–2700 (2023).

39. Mathiot, P., Jenkins, A., Harris, C. & Madec, G. Explicit representation and parametrised impacts of under ice shelf seas in the z∗ coordinate ocean model NEMO 3.6. *Geosci. Model Dev.* **10**, 2849–2874 (2017).

40. Walin, G. On the relation between sea-surface heat flow and thermal circulation in the ocean. *Tellus* **34**, 187–195 (1982).

41. Groeskamp, S. et al. The water mass transformation framework for ocean physics and biogeochemistry. *Annu. Rev. Mar. Sci.* **11**, 271–305 (2019).

42. Bailey S. T., Jones C. S., Abernathey R. P., Gordon A. L., Yuan X. Water mass transformation variability in the Weddell Sea in Ocean Reanalyses. *Ocean Sci.* **19**, 381-402 (2023).

43. Gordon, A. L. et al. Western Ross Sea continental slope gravity currents. *Deep Sea Res. Part II: Top. Stud. Oceanogr.* **56**, 796–817 (2009).

44. Williams G. et al. Antarctic bottom water from the Adélie and George V Land coast, East Antarctica (140–149 E). *J. Geophys. Res.: Oceans* **115**, C04027 (2010).

45. Bromwich, D. H. & Kurtz, D. D. Katabatic wind forcing of the Terra Nova Bay polynya. *J. Geophys. Res.: Oceans* **89**, 3561–3572 (1984).

46. Massom, R., Harris, P., Michael, K. J. & Potter, M. The distribution and formative processes of latent-heat polynyas in East Antarctica. *Ann. Glaciol.* **27**, 420–426 (1998).

47. Van Achter, G. et al. Modelling landfast sea ice and its influence on ocean–ice interactions in the area of the Totten Glacier, East Antarctica. *Ocean Model.* **169**, 101920 (2022).

48. Nihashi, S. & Ohshima, K. I. Circumpolar mapping of Antarctic coastal polynyas and landfast sea ice: relationship and variability. *J. Clim.* **28**, 3650–3670 (2015).

49. Fraser, A. D. et al. Landfast ice controls on sea-ice production in the Cape Darnley Polynya: a case study. *Remote Sens. Environ.* **233**, 111315 (2019).

50. Ohshima, K. I., Nihashi, S. & Iwamoto, K. Global view of sea-ice production in polynyas and its linkage to dense/bottom water formation. *Geosci. Lett.* **3**, 1–14 (2016).

51. Tamura, T., Williams, G., Fraser, A. & Ohshima, K. Potential regime shift in decreased sea ice production after the Mertz Glacier calving. *Nat. Commun.* **3**, 826 (2012).

52. Drucker R., Martin S., Kwok R. Sea ice production and export from coastal polynyas in the Weddell and Ross Seas. *Geophys. Res. Lett.* **38**, L17502 (2011).

53. Nakata, K., Ohshima, K. & Nihashi, S. Mapping of active frazil for Antarctic coastal polynyas, with an estimation of sea-ice production. *Geophys. Res. Lett.* **48**, e2020GL091353 (2021).

54. Stroeve, J. C., Schroder, D., Tsamados, M. & Feltham, D. Warm winter, thin ice? *Cryosphere* **12**, 1791–1809 (2018).

55. Petty, A. A., Holland, M. M., Bailey, D. A. & Kurtz, N. T. Warm Arctic, increased winter sea ice growth? *Geophys. Res. Lett.* **45**, 922–912,930 (2018).

56. Grose, M. R. et al. Insights from CMIP6 for Australia's future climate. *Earth's Future* **8**, e2019EF001469 (2020).

57. Purich, A. & England, M. H. Historical and future projected warming of Antarctic Shelf Bottom Water in CMIP6 models. *Geophys, Res. Lett.* **48**, e2021GL092752 (2021).

58. Lee J.-Y. et al. Future global climate: scenario-based projections and near-term information. *In*: Climate change 2021: The physical science basis. Contribution of working group I to the sixth assessment report of the intergovernmental panel on climate change). Cambridge University Press (2021).

59. Smedsrud, L. H. Warming of the deep water in the Weddell Sea along the Greenwich meridian: 1977–2001. *Deep Sea Res. Part I: Oceanogr. Res. Pap.* **52**, 241–258 (2005).

60. Lüpkes C., Gryanik V. M., Hartmann J., Andreas E. L. A parametrization, based on sea ice morphology, of the neutral atmospheric drag coefficients for weather prediction and climate models. *J. Geophys. Res.: Atmos.* **117**, D13112 (2012).

61. Orsi, A. H., Smethie, W. M. Jr & Bullister, J. L. On the total input of Antarctic waters to the deep ocean: a preliminary estimate from chlorofluorocarbon measurements. *J. Geophys. Res.: Oceans* **107**, 31-31–31-14 (2002).

62. Wang, X. et al. Impacts of strong wind events on sea ice and water mass properties in Antarctic coastal polynyas. *Clim. Dyn.* **57**, 3505–3528 (2021).

63. Dalaiden, Q., Goosse, H., Lenaerts, J. T., Cavitte, M. G. & Henderson, N. Future Antarctic snow accumulation trend is dominated by atmospheric synoptic-scale events. *Commun. Earth Environ.* **1**, 62 (2020).

64. Tewari, K., Mishra, S. K., Salunke, P. & Dewan, A. Future projections of temperature and precipitation for Antarctica. *Environ. Res. Lett.* **17**, 014029 (2022).

65. Pauling, A. G., Bitz, C. M., Smith, I. J. & Langhorne, P. J. The response of the Southern Ocean and Antarctic sea ice to freshwater from ice shelves in an Earth system model. *J. Clim.* **29**, 1655–1672 (2016).

66. Lago, V. & England, M. H. Projected slowdown of Antarctic bottom water formation in response to amplified meltwater contributions. *J. Clim.* **32**, 6319–6335 (2019).

67. Danabasoglu, G. et al. The community earth system model version 2 (CESM2). *J. Adv. Model. Earth Syst.* **12**, e2019MS001916 (2020).

68. Neale, R. B. et al. Description of the NCAR community atmosphere model (CAM 5.0). *NCAR Tech Note NCAR/TN-486 + STR* **1**, 1–12 (2010).

69. Smith, R. D. & Gent, P. R. Reference Manual for the Parallel Ocean Program (POP), Ocean Component of the Community Climate System Model (CCSM2.0 and 3.0) Technical Report LA-UR-02-2484 (Los Alamos National Laboratory, 2002).

70. Lawrence D. M. et al. Parameterization improvements and functional and structural advances in version 4 of the community land model. *J. Adv. Model. Earth Syst.* https://doi.org/10.1029/2011ms00045 (2011).

71. Hunke, E. C., Lipscomb, W. H., Turner, A. K., Jeffery, N. & Elliott, S. Cice: the los alamos sea ice model documentation and software user's manual version 4.1 la-cc-06-012. *T-3 Fluid Dynamics Group, Los Alamos National Laboratory* **675**, 500 (2010).

72. Small, R. J. et al. A new synoptic scale resolving global climate simulation using the Community Earth System Model. *J. Adv. Model. Earth Syst.* **6**, 1065–1094 (2014).

73. Turner, J., Bracegirdle, T. J., Phillips, T., Marshall, G. J. & Hosking, J. S. An initial assessment of Antarctic sea ice extent in the CMIP5 models. *Journal of Climate* **26**, 1473–1484 (2013).

74. Zunz, V., Goosse, H. & Massonnet, F. How does internal variability influence the ability of CMIP5 models to reproduce the recent trend in Southern Ocean sea ice extent? *Cryosphere* **7**, 451–468 (2013).

75. Gagné, M. È., Gillett, N. & Fyfe, J. Observed and simulated changes in Antarctic sea ice extent over the past 50 years. *Geophys. Res. Lett.* **42**, 90–95 (2015).

76. Shu, Q. et al. Assessment of sea ice extent in CMIP6 with comparison to observations and CMIP5. *Geophys. Res. Lett.* **47**, e2020GL087965 (2020).

77. Roach, L. A. et al. Antarctic sea ice area in CMIP6. *Geophys. Res. Lett.* **47**, e2019GL086729 (2020).

78. Rackow, T. et al. Delayed Antarctic sea-ice decline in high-resolution climate change simulations. *Nat. Commun.* **13**, 637 (2022).

79. Chung, E.-S. et al. Antarctic sea-ice expansion and Southern Ocean cooling linked to tropical variability. *Nat. Clim. Change* **12**, 461–468 (2022).

80. Locarnini M. et al. World Ocean Atlas 2018, volume 1: Temperature. (2018).

81. Zweng M. et al. World Ocean Atlas 2018, volume 2: Salinity. (2019).

82. Fetterer F., Knowles K., Meier W., Savoie M., Windnagel A. Sea Ice Index. Version 3 [updated daily]. NSIDC: National Snow and Ice Data Center, Boulder, Colorado, USA.) (2017).

83. Cavalieri D. J., Parkinson C., Gloersen P., Zwally H. J. Sea ice concentrations from Nimbus-7 SMMR and DMSP SSM/I-SSMIS passive microwave data). Version (1996).

84. Foldvik A., et al. Ice shelf water overflow and bottom water formation in the southern Weddell Sea. *J. Geophys. Res.: Oceans* **109**, C02015 (2004).

Author contributions

H.-S.P. and H.J. designed the study. H.J. conducted the analysis and wrote the initial manuscript draft under the guidance of H.-S.P. and A.L.S. S.-S.L. conducted the CESM1.2.2 high-resolution simulations. All authors contributed to the interpretation of results and the writing.

Competing interests

The authors declare no competing interests.

Additional information

Supplementary information The online version contains supplementary material available at https://doi.org/10.1038/s43247-023-01156-y.

Correspondence and requests for materials should be addressed to Hyo-Seok Park.

Peer review information *Communications Earth & Environment* thanks Cara Nissen, Carmela Veneziani, and the other, anonymous, reviewer(s) for their contribution to the peer review of this work. Primary Handling Editors: Shin Sugiyama, Heike Langenberg. Peer reviewer reports are available.

Reprints and permission information is available at http://www.nature.com/reprints

Publisher's note Springer Nature remains neutral with regard to jurisdictional claims in published maps and institutional affiliations.